# Scaling of Dynamic Contact Angles in a Lattice-Boltzmann Model

M. Latva-Kokko and Daniel H. Rothman

*Department of Earth, Atmospheric, and Planetary Sciences, Massachusetts Institute of Technology,*
*77 Massachusetts Avenue, Cambridge, Massachusetts 02139-4307, USA*

(Received 22 April 2006; published 19 June 2007)

We study the origins of the dynamic contact angle in a two-dimensional lattice-Boltzmann model of immiscible fluids. We show that the dynamic contact angle changes as a function of capillary number as observed in laboratory experiments and explain how this dependence arises in the lattice-Boltzmann model. We also explain how the fluid-fluid interface can move while retaining its shape. The interface has an apparent slip length. The apparent slip follows the classical Navier slipping rule where the velocity of the fluid at the wall is proportional to the viscous stress at the wall. This apparent slip length is proportional to the viscous length scale associated with the spurious flow induced by uncompensated stress at the three-phase contact point.

DOI: 10.1103/PhysRevLett.98.254503 PACS numbers: 47.11.−j, 47.55.−t, 68.08.−p

When the interface between two immiscible fluids moves through a capillary tube, the angle of contact formed by the fluid interface with the solid wall is observed to vary with velocity, viscosity, and surface tension [1–15]. This variation in the *dynamic contact angle*, $\theta_{\rm dyn}$ appears to follow precise empirical relationships [1,2,13–15], the foundations of which remain only partially understood [2–5,9,16]. The main difficulty lies in the breakdown of the celebrated "no-slip" boundary condition of continuum fluid mechanics [17–19]. The specification of no-slip at the three-phase contact line would imply infinite drag [5,7,8], yet the interface moves. The dynamic nature of the contact angle is likely related to this conundrum [3,9,11,12].

One of the more profound theoretical predictions of the dynamic contact angle is due to Cox [3]. In his work he used a general slip model and matched asymptotic expansions involving the dynamic contact angle. Other possible explanations include rolling motion [6,7], a thin precursor film [4,5], stick-slip behavior [4,11,20], and a diffuse interface [21–24]. Here we study the dynamic contact angle using a lattice-Boltzmann (LB) model. Our results show that the macroscopic dynamics involving the dynamic contact angle and apparent slip as predicted by the Cox model [3] are obtainable with a minimal mass- and momentum-conserving lattice dynamics without specifying a slip length. Instead, an *effective* slip length arises from the microscopic dynamics. The simplicity of our LB model allows the origin of this microscopic-macroscopic link to be fully characterized, thereby showing how the phenomenology of the dynamic contact angle can arise in a microscopic hydrodynamic model.

For a fluid of viscosity $\eta$, flow velocity $v$, and surface tension $\gamma$ flowing in a capillary tube of aperture $L$, the dynamic contact angle $\theta_{\rm dyn}$ depends on three dimensionless parameters: the capillary number ${\rm Ca} = \frac{\eta}{\gamma} v$, the phenomenological slip length $l_s/L$, and static contact angle $\theta$. If a system exhibits contact angle hysteresis, $\theta$ should be replaced by the advancing contact angle $\theta_a$ [4,13,14]. In his pioneering paper, Hoffman [1] showed that the dynamic contact angle follows the universal relation

$${\rm Ca} = F(\theta_{\rm dyn}) - F(\theta_a), \tag{1}$$

where $F$ is a scaling function. Cox later derived a relation in a general slip model [3],

$$G(\theta_{\rm dyn}) = G(\theta_a) + {\rm Ca} \log(L/l_s), \tag{2}$$

to lowest order in Ca and $l_s/L$. He also gives an analytical expression for the function $G$. Sheng and Zhou show that Eq. (2) is approximated well by [9]

$$\cos\theta_a - \cos\theta_{\rm dyn} = {\rm Ca} \log(KL/l_s), \tag{3}$$

where $K$ is a constant. Sheng and Zhou further show that this same relation holds for a number of different slip models. The only thing that changes is the value of the constant $K$. One of the slip models that Sheng and Zhou use is the so-called Navier model [5,9,18]. In this slip model the slipping velocity of the fluid at the wall is proportional to the viscous stress, i.e., $v_x = \beta\sigma_{xy} = (l_s/\eta)\sigma_{xy}$, where $\beta = 0$ for no slip.

In the following we first show that the scaling of $\theta_{\rm dyn}$ predicted by Eqs. (2) and (3) is exhibited in our simulations and then discuss the origin of this scaling in the LB model. We will also show that the slipping mechanism falls into the general-class of Navier slip models. The fundamental idea of the LB method [25–28] is to construct simplified kinetic models from a discrete finite set of particle velocities such that, at macroscopic length and time scales, the Navier-Stokes equations are asymptotically recovered. In an LB model the particle populations $N_i^\sigma(\mathbf{x}, t)$, which give the velocity pressure and stress at a fluid element, are first propagated in lattice directions $\mathbf{c}_i$ [25–28], and then they relax toward pseudoequilibrium distributions $N_i^{\rm eq}(\mathbf{x}, t)$ [25,28]. We use single-relaxation time lattice Bhatnagar-Gross-Krook (BGK) model [25]. In this model, the post-collision state is given by $N_i'(\mathbf{x}, t) = (1 + \lambda)N_i(\mathbf{x}, t) - \lambda N_i^{(\rm eq)}(\mathbf{x}, t)$, where the relaxation parameter $\lambda$ determines the kinematic viscosity $\nu = \eta/\rho$: [28]

$$\nu = -\frac{1}{3}\left(\frac{1}{\lambda} - \frac{1}{2}\right). \tag{4}$$

We use a simple bounce-back rule [25,29] on the walls. This rule leads to a no-slip boundary condition [25,29]. The wetting tendency of the walls is controlled by a single parameter [30]. The surface tension and interfacial dynamics are incorporated with the use of the color gradient [25,30–32] $\mathbf{f}(\mathbf{x}, t) = \sum_i \mathbf{c}_i \sum_j [N_j^{\text{red}}(\mathbf{x} + \mathbf{c}_i, t) - N_j^{\text{blue}}(\mathbf{x} + \mathbf{c}_i, t)]$. The color gradient acts as a proxy for the orientation of the interface. The lattice distributions are changed according to [30,31]

$$N_i''(\mathbf{x}, t) = N_i'(\mathbf{x}, t) + A|\mathbf{f}(\mathbf{x}, t)|\left[\frac{(\mathbf{c}_i \cdot \mathbf{f})^2}{\mathbf{f} \cdot \mathbf{f}} - \frac{1}{2}\right] \tag{5}$$

to include the effect of surface tension. The parameter $A$ determines the surface tension $\gamma = \frac{-192\rho A}{\lambda}$ [25,30].

Each simulation is initalized with red fluid invading the blue fluid in a two-dimensional straight and smooth channel. The walls are chosen to be neutrally wetting so that the static contact angle $\theta$ is 90 degrees; as shown previously, our model yields $\theta_a = \theta$ [30]. In Fig. 1 we show the steady-state interfacial shapes for capillary numbers ranging from $6.72 \times 10^{-3}$ to $3.12 \times 10^{-2}$. We measure the dynamic contact angle by measuring the radius of curvature of the interface at the center of the channel [9,30]. Close to the wall the viscous stresses are comparable to the capillary pressure and hence the interface bends [9].

In Fig. 2 we show the measured dynamic contact angles as a function of capillary number. As expected, the dynamic contact angle increases as the capillary number is increased. For any given set of the simulation parameters $L$, $\nu$, and $A$, the excess curvature $\cos\theta_a - \cos\theta_{\text{dyn}}$ depends linearly on the capillary number. However, if any of the simulation parameters change, the proportionality factor also changes. These curves collapse to a single line if one instead plots $\cos\theta_a - \cos\theta_{\text{dyn}}$ as a function of $\text{Ca}\log(AL/A_0\nu)$. Comparing with Eq. (3) we find the same relationship but with $\nu A_0/A$ playing the role of the slip length $l_s$. Here $A_0 = 3.162 \times 10^{-4}$ is a scale factor for surface tension. We find this scale factor by least square fit with $A_0$ being the free parameter.

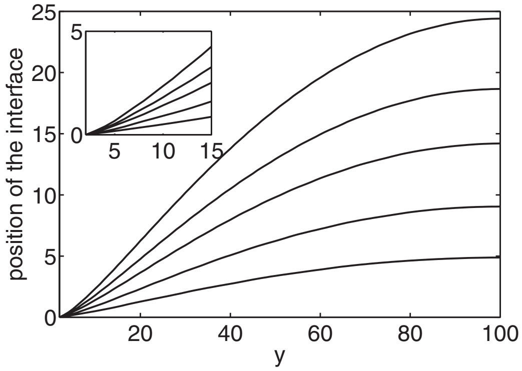

FIG. 1. We show the shape of the fluid-fluid interface in a $L = 200$ size tube. These curves are for $\theta_a = 90°$, i.e., neutral wetting, and for capillary numbers $6.72 \times 10^{-2}$, $1.23 \times 10^{-2}$, $1.89 \times 10^{-2}$, $2.46 \times 10^{-2}$, and $3.12 \times 10^{-2}$ from bottom to top. In the inset we show the shape of the interface close to the wall. One can see that the apparent contact angle changes toward $\theta_a$ and that the dynamic contact angle needs to be measured at the central part of the flow where the interface is essentially rigid with respect to the flow.

To gain a better understanding of the dynamic contact angle and the apparent slip at the contact point we investigate the lattice dynamics near the three-phase contact point. At the corner sites (i.e., sites neighboring both the wall and the fluid-fluid interface) the direction of the color gradient is neither the direction of the fluid-fluid interface nor the direction of the wall. The equilibrium distributions are perturbed such that the directions parallel to the color gradient receive more particles and directions perpendicular to it receive less. This introduces a stress to the fluid elements. This stress mimics the surface tension [25,30] for

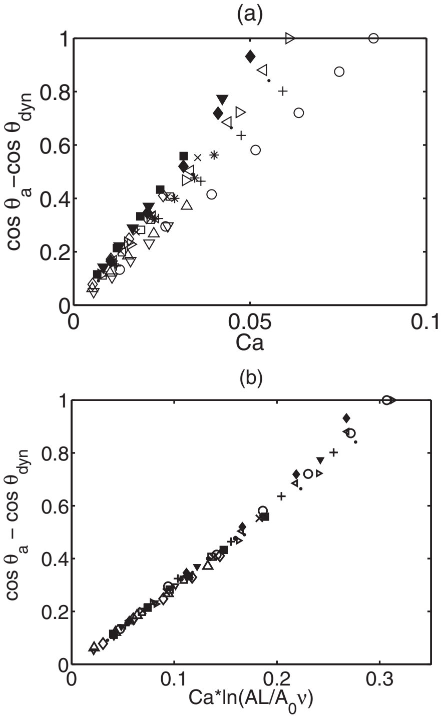

FIG. 2. (a) The dynamic contact angle as a function of capillary number. (b) The same data rescaled as a function of $\text{Ca}\log(AL/A_0\nu)$. The data points give the measured dynamic contact angle in a LB simulation. The markers show different simulation conditions: ∘: $A = 10^{-4}$, $\nu = 1/3$, $L = 50$; +: $A = 10^{-4}$, $\nu = 1/6$, $L = 50$; *: $A = 2 \times 10^{-4}$, $\nu = 1/6$, $L = 50$; □: $A = 4 \times 10^{-4}$, $\nu = 1/6$, $L = 50$; ×: $A = 6 \times 10^{-4}$, $\nu = 1/6$, $L = 50$; •: $A = 10^{-4}$, $\nu = 1/12$, $L = 50$; ◇: $A = 10^{-4}$, $\nu = 1/24$, $L = 50$; ▽: $A = 10^{-4}$, $\nu = 1/6$, $L = 30$; △: $A = 2 \times 10^{-4}$, $\nu = 1/6$, $L = 30$; ◁: $A = 10^{-4}$, $\nu = 1/6$, $L = 70$; ▷: $A = 10^{-4}$, $\nu = 1/6$, $L = 70$; ◆: $A = 10^{-4}$, $\nu = 1/6$, $L = 100$; ▲: $A = 10^{-4}$, $\nu = 1/6$, $L = 150$; ■: $A = 10^{-4}$, $\nu = 1/6$, $L = 200$.

flat and moderately curved interfaces. However, at the corner node the direction of the color gradient changes abruptly. This stress cannot be compensated with an increase in pressure near the corner node. Instead, it induces a flow where particles flow towards the corner node along the interface and away from it along the wall.

To demonstrate the effect of the uncompensated stress component we initialize a lattice of size $100 \times 50$ lattice sites. We choose the relaxation parameter $\lambda = -1.0$ and surface tension parameter $A = 10^{-4}$. The wall is left neutrally wetting. This will recover an immobile flat interface. However, due to spurious currents [25,33] the fluid is not at rest. In Fig. 3(a) we show the resulting flow pattern. The uncompensated stress at the three-phase contact point induces a circular flow pattern. In Fig. 3(b) we show the flow pattern in a comoving frame when the average fluid velocity $v_x = 2.73 \times 10^{-3}$ lattice units per time step. This pattern is reminiscent of the rolling motion [3,6,7]. It is slightly different, however, from the flow patterns reported by Dussan [7] and Sheng and Zhou [9]. In our simulations the flow in the slip region has a circulation pattern in front of the moving interface instead of behind it. This is because the flow velocity tangential to the interface is directed towards the wall rather than away from it.

To determine how these currents are generated, we plot the extrapolated $x$-directional wall velocity in Fig. 4. This is found by a cubic fit of $v_x$ near the wall and extrapolation to the expected wall position between the first fluid node and the wall node. This velocity results from the uncompensated stresses at the three-phase contact point. We further test how the extrapolated wall velocity changes as the average flow velocity $\bar{v}_x$, the system size $L$, the surface tension, and viscosity are varied. As $\bar{v}_x$ changes the wall velocity remains constant. This is a clear indication that even for a moving fluid and hence a moving interface the unbalanced stress component at the three-phase contact point induces a constant velocity field that is then superimposed on the flow. As $L$ changes the wall velocity also remains constant. Changing the viscosity does not change the maximal velocity, but it does change $v_x(x)$ (and hence the flow pattern) due to viscous damping. Figure 4 shows the wall velocity for four different values of the surface tension (solid line). As $A$ is increased, the wall velocity increases in linear fashion. We also show the viscous stress $\sigma_{xy}$ for the same values of $A$. The inset shows the Navier slipping relation, $v_x = \beta \sigma_{xy}$, is followed where the proportionality factor $\beta$ is constant. Since $\beta = l_s/\eta$ in the Navier model the slipping length suggested by this model must be proportional to the viscosity.

The fact that the circulation pattern is superimposed on the flow explains how the contact line moves while keeping its shape constant. The circulation allows for rolling motion over the solid surface. Away from the interface (approximately 20 lattice sites in front and behind) we have the usual parabolic flow profile. As we move closer to the interface the flow profile becomes progressively flatter. This confirms the conclusion of Sheng and Zhou [9] that, far from the wall, at the interface the viscous stress is significantly smaller than the capillary pressure. Hence at the center of a capillary tube the interface appears rigid to the fluid and moves as a plug with constant velocity. Close to the walls, however, the viscous stresses increase and the interface is deformed (see Fig. 1). This forces the dynamic contact angle to deviate from $\theta_a$. This change is linearly proportional to the capillary number. The proportionality factor of this change is, however, model dependent. In slip models [1,3,9] the proportionality factor depends on the slip length as given by Eq. (3). The uncompensated stress component at the three-phase contact point induces a flow that has maximum velocity $u_{\max} = \text{const} \times A$. There is a viscous length scale $l_s$ associated with this flow. In lattice units,

$$l_{\text{visc}} = \frac{\eta}{\rho u_{\max}} = \frac{\nu}{u_{\max}} = \text{const} \times \frac{\nu}{A}. \tag{6}$$

From Eq. (3) and Fig. 2(a) we thus find that $l_s = \text{constant} \times l_{\text{visc}}$. Because $l_{\text{visc}}$ is the only nontrivial intrinsic length scale in our LB model, it is not surprising that it is related to $l_s$. Of course, $l_s = l_{\text{visc}}$ is not expected for real fluids. The main point, however, is that the uncompensated

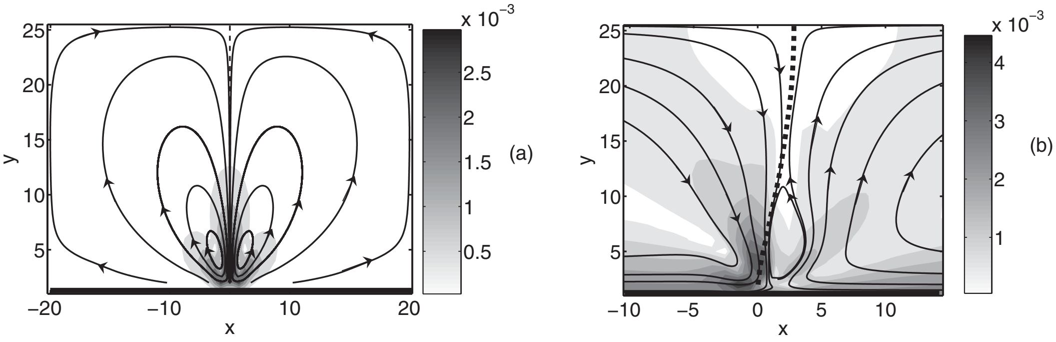

FIG. 3. (a) The flow lines in the bottom half of $100 \times 50$ lattice sites. The wall is marked with a solid line at $y = 0$ and the interface with a dashed line at $x = 0$. The flow circulates around the lattice and is induced by the stresses at the three-phase contact point. (b) Flow lines in a comoving frame for flow velocity $v_x = 2.73 \times 10^{-3}$. The gray scale gives the magnitude of the flow velocity in both plots.

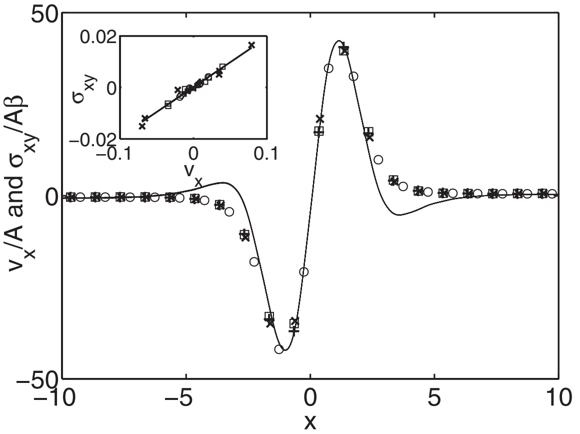

FIG. 4. Solid line: the $x$ component of velocity for $A = 5 \times 10^{-5}$, $10^{-4}$, $2 \times 10^{-4}$, $4 \times 10^{-4}$. This line represents all four values of $A$. As $A$ increases the velocity increases linearly, but the rescaled curve $v_x/A$ remains the same. Symbols: the stress component $\sigma_{xy}$ for the same values of $A$. In the inset the viscous stress $\sigma_{xy}$ as a function of the slipping velocity $v_x$, confirming that our LB model follows the Navier slipping relation.

stresses in our LB model result in a moving contact line phenomenology indistinguishable from real fluids.

In conclusion, we have shown how a microscopic hydrodynamic model reproduces the macroscopic physics of a moving contact line. We have found the dependence of $\theta_{\rm dyn}$ on the capillary number Ca and slip length $l_s$ and have shown that our LB model falls in the general class of Navier slipping models. Compared to the macroscopic model of Sheng and Zhou [9], we do not specify a slip length; the slip length instead arises as a result of the microscopic dynamics. Compared to molecular dynamics simulations [10–12] we show the slipping phenomenology in a simplified fluid, thereby indicating a possible set of minimal microscopic ingredients for moving contact line phenomena. In previous studies of moving contact lines in LB [21,22], the existence of an apparent slip length $l_s$ had been found, but the scaling of $\theta_{\rm dyn}$ and the nature of the slip condition had not been discussed. In our model, as in other LB models, we have particles with discrete velocities on a lattice. These particles conserve mass and momentum. The only extra ingredient we require is the uncompensated stress at the fluid-fluid-solid interface, which is a direct consequence of the surface tension imposed on the fluids. Despite the existence of spurious currents [25,33] the LB model exhibits the correct macroscopic phenomena. Our point is not to suggest that our model be used for engineering applications of contact line dynamics. Our results instead address the foundations of this problem. Without specification of a slip length, our LB model produces the same dynamics as the various slip models [5–9]. Thus a minimal macroscopic understanding of Nature's apparent "violation" of the no-slip boundary condition need not require an imposition of an artificial slip length.

This work was supported by the Office of Science (BER), US Department of Energy, Grant No. DE-FG07-02ER63490. We would like to extend our thanks to Alex Lobkovsky and David Forney for fruitful conversations and suggestions.

[1] R. L. Hoffman, J. Colloid Interface Sci. **50**, 228 (1975).
[2] L. Tanner, J. Phys. D **12**, 1473 (1979).
[3] R. G. Cox, J. Fluid Mech. **168**, 169 (1986).
[4] P. G. de Gennes, Rev. Mod. Phys. **57**, 827 (1985).
[5] V. E. Dussan, Annu. Rev. Fluid Mech. **11**, 371 (1979).
[6] L. M. Hocking, J. Fluid Mech. **76**, 801 (1976).
[7] V. E. Dussan and S. Davis, J. Fluid Mech. **65**, 71 (1974).
[8] C. Huh and L. E. Scriven, J. Colloid Interface Sci. **35**, 85 (1971).
[9] P. Sheng and M. Zhou, Phys. Rev. A **45**, 5694 (1992).
[10] J. Koplik, J. R. Banavar, and J. M. Willemsen, Phys. Rev. Lett. **60**, 1282 (1988).
[11] J. Koplik and J. R. Banavar, Annu. Rev. Fluid Mech. **27**, 257 (1995).
[12] W. Jin, J. Koplik, and J. Banavar, Phys. Rev. Lett. **78**, 1520 (1997).
[13] M. Fermigier and P. Jenffer, J. Colloid Interface Sci. **146**, 226 (1991).
[14] E. Schäffer and P. Wong, Phys. Rev. E **61**, 5257 (2000).
[15] J. P. Stokes *et al.*, Phys. Rev. Lett. **65**, 1885 (1990).
[16] J. F. Joanny and M. O. Robbins, J. Chem. Phys. **92**, 3206 (1990).
[17] S. Goldstein, Annu. Rev. Fluid Mech. **1**, 1 (1969).
[18] E. Lauga, M. P. Brenner, and H. A. Stone, arXiv:cond-mat/0501557.
[19] F. M. White, *Fluid Mechanics* (McGraw-Hill, New York, 1994).
[20] D. Ertas and M. Kardar, Phys. Rev. E **49**, R2532 (1994).
[21] A. J. Briant, A. J. Wagner, and J. M. Yeomans, Phys. Rev. E **69**, 031602 (2004).
[22] A. J. Briant and J. M. Yeomans, Phys. Rev. E **69**, 031603 (2004).
[23] D. Jacqmin, J. Fluid Mech. **402**, 57 (2000).
[24] H.-Y. Chen, D. Jasnow, and J. Viñals, Phys. Rev. Lett. **85**, 1686 (2000).
[25] D. H. Rothman and S. Zaleski, *Lattice-Gas Cellular Automata* (Cambridge University Press, Cambridge, England, 1997).
[26] G. R. McNamara and G. Zanetti, Phys. Rev. Lett. **61**, 2332 (1988).
[27] F. J. Higuera and J. Jimenez, Europhys. Lett. **9**, 663 (1989).
[28] Y. H. Qian, D. d'Humieres, and P. Lallemand, Europhys. Lett. **17**, 479 (1992).
[29] I. Ginzburg and P. M. Adler, J. Phys. II (France) **4**, 191 (1994).
[30] M. Latva-Kokko and D. H. Rothman, Phys. Rev. E **72**, 046701 (2005).
[31] M. Latva-Kokko and D. H. Rothman, Phys. Rev. E **71**, 056702 (2005).
[32] A. K. Gunstensen, D. H. Rothman, S. Zaleski, and G. Zanetti, Phys. Rev. A **43**, 4320 (1991).
[33] S. L. Hou, X. W. Shan, Q. S. Zou, G. D. Doolen, and W. E. Soll, J. Comput. Phys. **138**, 695 (1997).